Small

NANO · MICRO small
www.small-journal.com

RESEARCH ARTICLE OPEN ACCESS

A Label-Free Ultraviolet Photoacoustic Microscopy Enables Nuclear Imaging and Toxicity Assessment in an Intact Brain Organoid

Hyunjun Kye[1,2] | Won Jong Yu[3] | Lihong V. Wang[4] | Jeesu Kim[2] | Jong-Chan Park[1,3,5] | Byullee Park[1,3,5]

[1]Department of Biophysics, Institute of Quantum Biophysics, Sungkyunkwan University, Suwon, Republic of Korea | [2]Department of Cogno-Mechatronics Engineering, Pusan National University, Busan, Republic of Korea | [3]Department of MetaBioHealth, Sungkyunkwan University, Suwon, Republic of Korea | [4]Caltech Optical Imaging Laboratory, Andrew and Peggy Cherng Department of Medical Engineering, California Institute of Technology, Pasadena, California, USA | [5]Department of Biopharmaceutical Convergence, Sungkyunkwan University, Suwon, Republic of Korea

Correspondence: Lihong V. Wang (LVW@caltech.edu) | Jeesu Kim (jeesukim@pusan.ac.kr) | Jong-Chan Park (jongchan@g.skku.edu) | Byullee Park (byullee@skku.edu)

Received: 26 January 2026 | **Revised:** 18 June 2026 | **Accepted:** 2 July 2026

Keywords: brain organoid | label-free imaging | photoacoustic microscopy | single cell imaging

ABSTRACT

Fetal alcohol spectrum disorders (FASDs) are caused by prenatal exposure to ethanol (EtOH), leading to developmental brain abnormalities. Cortical organoids derived from human-induced pluripotent stem cells provide physiologically relevant models to study such neurotoxic effects. However, accurate imaging of nuclear morphology, a key indicator of cytotoxicity and developmental impairment, remains difficult. Traditional fluorescence-based techniques rely on staining and sectioning, limiting throughput and potentially altering native structures. Herein, we present an ultraviolet photoacoustic microscopy system that targets endogenous nucleic acids at 266 nm excitation, resulting in a lateral resolution of 278 nm, which is sufficient to resolve individual nuclei in situ. The system integrates precise z-axis scanning for focal-plane alignment, enabling high-resolution depth-resolved imaging of subvolumes within 3D intact live organoids without physical sectioning. Using EtOH-treated cortical organoids as a model of FASD-associated neurotoxicity, we observed significant reductions in nuclear area, diameter, and circularity by 46.1%, 20.8%, and 6.0%, respectively, indicating structural damage consistent with apoptosis and impaired neurodevelopment. This method is the first to demonstrate label-free nuclear imaging in intact live brain organoids, providing a robust and preparation-free platform for probing disease-relevant phenotypes, accelerating drug screening, and enabling early toxicity assessments in neurodevelopmental disorder models.

1 | Introduction

Prenatal exposure to neurotoxic agents such as ethanol (EtOH) is a major contributor to developmental brain disorders, including fetal alcohol spectrum disorders (FASDs) [1–4]. These conditions are associated with disrupted neurogenesis, impaired neuronal migration, and long-term cognitive deficits [5]. Understanding the cellular basis of EtOH-induced neurotoxicity is critical for early-stage drug testing and developmental toxicity assessment [6]. However, traditional in vivo models have limitations owing to species differences and ethical concerns [7, 8]. In this context, cortical organoids, which are 3D structures derived from

Hyunjun Kye and Won Jong Yu contributed equally to this work.

human-induced pluripotent stem cells (hiPSCs), have emerged as physiologically relevant platforms that recapitulate key aspects of human neurodevelopment [9, 10]. Cortical organoids were established by reprogramming patient-derived peripheral blood mononuclear cells or fibroblasts into hiPSCs, followed by embryoid body (EB) formation, neuronal differentiation, and long-term maturation (Figure 1a). These organoids were subsequently utilized for downstream applications, including drug screening, high-content imaging, and analysis, to support precision therapy. By exhibiting multicellular organization, spatial patterning, and dynamic cell–cell interactions, cortical organoids enable more accurate modeling of human-specific neurotoxicity and disease mechanisms than 2D cultures or animal models [11–14].

The accurate assessment of neurotoxic effects in organoid models requires reliable imaging of nuclear morphology, which serves as a key indicator of cellular stress, apoptosis, and developmental impairment [2, 15, 16]. Fluorescence-based microscopy techniques such as widefield, confocal, and multiphoton microscopy have been widely used for this purpose because of their high sensitivity, molecular specificity, and subcellular resolution [17–19]. However, these techniques depend on exogenous labeling and frequently require physical sectioning or optical clearing, which introduce sample perturbation, procedural complexity, and experimental variability [20, 21]. Moreover, the large size and scattering nature of organoids limit imaging depth and resolution in intact samples, hindering the accurate assessment of cellular structures in their native environment (Figure 1b) [22, 23].

To address these limitations, label-free imaging methods that provide subcellular resolution while preserving the native structure of organoids are highly desirable. Photoacoustic microscopy (PAM) provides such a solution by detecting optical absorption from endogenous chromophores, which induces localized thermoelastic expansion and generates broadband photoacoustic (PA) signals that are subsequently detected by an ultrasound transducer (Figure 1c) [24], allowing for noninvasive visualization of biological structures [25–31]. Ultraviolet PAM (UV-PAM) leverages the strong absorption of nucleic acids at 266 nm to image cell nuclei without staining or tissue processing. Previous applications have primarily focused on nuclear density or overall cell counts within tissues [20, 32–36]. However, detailed assessments of single-nucleus morphological changes are limited. Therefore, there is a need for imaging techniques with improved resolution that can capture changes in the individual nuclear architecture.

Herein, we present the first use of UV-PAM to assess drug-induced cytotoxicity in intact live cortical organoids. We developed a z-scanning UV-PAM (UV-PAM-Z) system that integrates a piezoelectric stage with a 0.5 μm step size for precise focal-plane alignment, facilitating depth-resolved subvolume imaging of subcellular nuclear morphology. The system achieves a lateral resolution of 278 nm, enabling subcellular imaging of individual nuclei. Using this system, we imaged subvolumes of non-sectioned cortical organoids treated with EtOH, a known teratogen and neurotoxic agent, and observed significant reductions in nuclear size and area. These alterations reflect structural damage consistent with apoptosis and impaired neurodevelopment. Finally, the alcoholic challenge experiment revealed distinct nuclear morphological changes between control and EtOH-treated organoids (Figure 1d), highlighting the capability of UV-PAM to detect EtOH-induced cellular damage in a label-free and physiologically relevant manner. Our results demonstrate the utility of UV-PAM-Z as a preparation-free, high-resolution platform for assessing neurotoxicity in physiologically relevant 3D brain tissue models.

2 | Results

2.1 | UV-PAM-Z System Characterization and Performance Evaluation

To achieve high-resolution and label-free PA imaging, we developed a UV-PAM-Z system optimized for operation at 266 nm. The UV-PAM-Z system was configured as a transmission-mode PAM incorporating a pulsed UV laser (Figure 2a). A z-axis piezo stage mounted with an objective lens was incorporated for fine axial scanning and focal alignment. This allows precise focus adjustments with a step size of 0.5 μm. This integrated optical-acoustic platform allows depth-resolved imaging of 3D samples without the need for staining or sectioning.

Phantom experiments were performed to characterize the spatial resolution of the UV-PAM-Z system. Lateral and axial resolutions were measured using a gold nanoparticle (GNP, 100 nm diameter) and a carbon fiber (6–8 μm diameter), respectively. Representative PA B-mode images of the two targets are shown in Figure S1. The lateral resolution was characterized from the PA B-mode image of the GNP target. Gaussian fitting of the lateral PA intensity profile yielded a full width at half maximum (FWHM) of 278 nm (Figure 2b). After correcting for the particle size, the lateral resolution was estimated to be 257 nm, which was in good agreement with the theoretical value of 247 nm (Note S1). The axial resolution was characterized from the PA B-mode image of the carbon-fiber target. Gaussian fitting of the envelope of the corresponding PA A-line signal yielded an axial resolution of 25.6 μm (Figure 2c). To validate this result, the frequency spectrum of the corresponding PA signal was analyzed (Figure 2d) and compared with the pulse-echo response of the ultrasound signal (Figure S2). The PA signal exhibited a center frequency of 39.5 MHz and a −6 dB bandwidth of 57.0 MHz, comparable to the pulse-echo bandwidth of 59.5 MHz. Based on these bandwidths, the theoretical axial resolutions were estimated to be 23.2 and 22.2 μm, respectively (Note S2). These values were in good agreement with the experimentally measured axial resolution, confirming the reliability of the axial resolution measurement.

We conducted a depth-scanning experiment using a tilted carbon-fiber sample to evaluate the z-axis imaging performance of the UV-PAM-Z system. This test aimed to verify whether the PA focus accurately followed the displacement of the piezo stage. The piezo stage was operated in the open-loop mode, resulting in a displacement of 1.67 μm per volt. When the focus was aligned with the top surface of the quartz glass (z = 0 μm), the reference voltage was set to 140 V. As the voltage decreased, the focus shifted upward along the z-axis. As shown in Figure 2e, one end of the carbon fiber was fixed to the surface of the quartz glass, while the other end was attached at a tilted position of 1.2 mm along the y-axis and 200 μm along the z-axis. The 1.2 mm distance was measured from a black tape landmark, while the 200 μm elevation was achieved using a quartz glass layer.

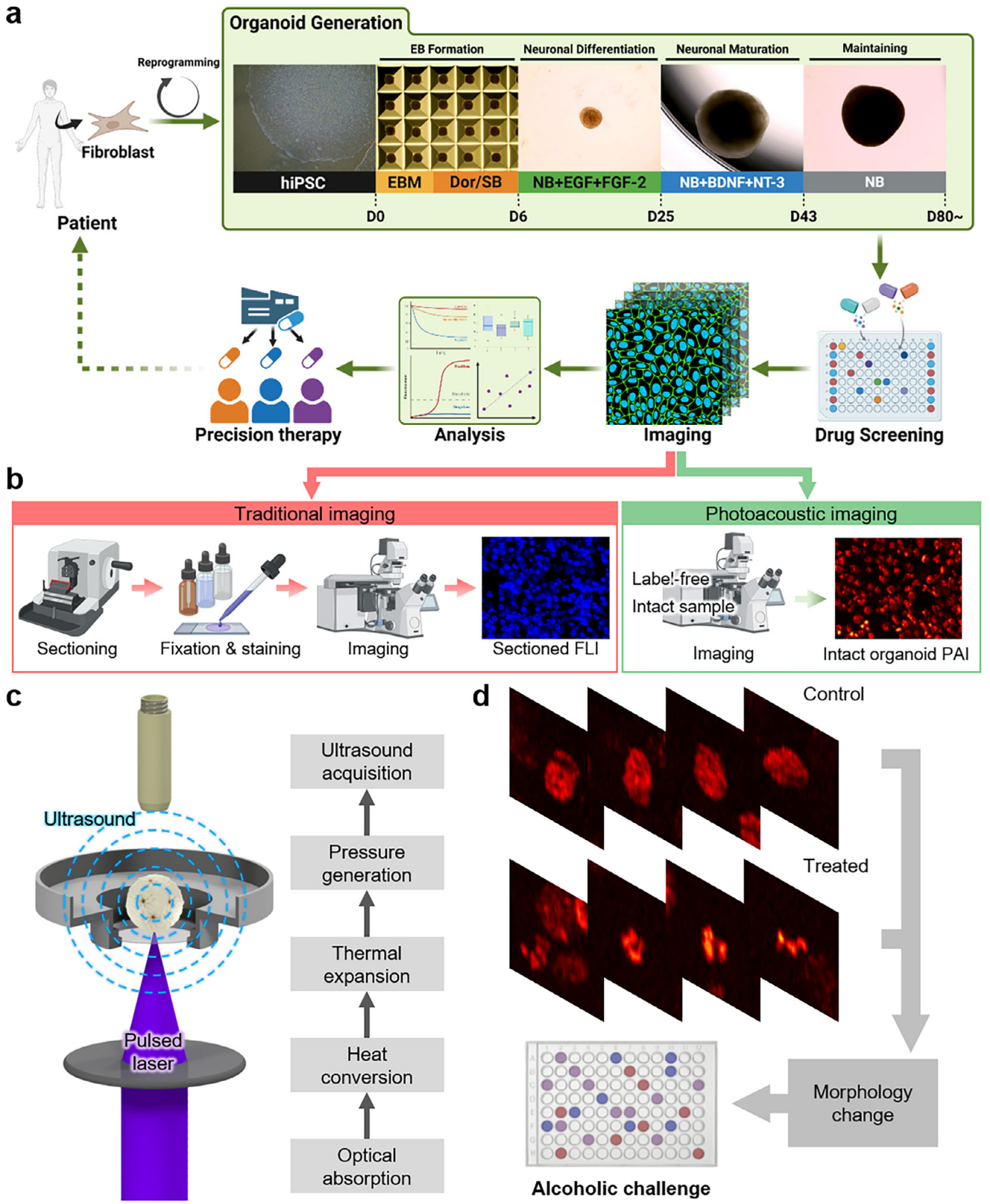

FIGURE 1 | Schematic illustration of organoid generation and UV-PAM-Z imaging workflow. (a) Protocol for forebrain organoid generation and its potential applications. (b) Comparison between traditional fluorescence imaging, which requires sectioning and labeling, and label-free UV-PAM-Z imaging of intact organoids. (c) Working principle of UV-PAM-Z imaging based on pulsed laser excitation and ultrasound detection. (d) Alcoholic challenge experiments with control and EtOH-treated organoids, showing nuclear morphological differences using UV-PAM-Z. PBMC, peripheral blood mononuclear cell; hiPSC, human induced pluripotent stem cell; EB, embryoid body; EBM, embryoid body formation medium; Dor, dorsomorphin; SB, SB431542; NB, Neurobasal medium; EGF, epidermal growth factor; FGF-2, basic fibroblast growth factor; BDNF, brain-derived neurotrophic factor; NT3, neurotrophin-3; D, day; FLI, fluorescence imaging; PAI, photoacoustic imaging; UV-PAM-Z, z-scanning UV photoacoustic microscopy; EtOH, ethanol.

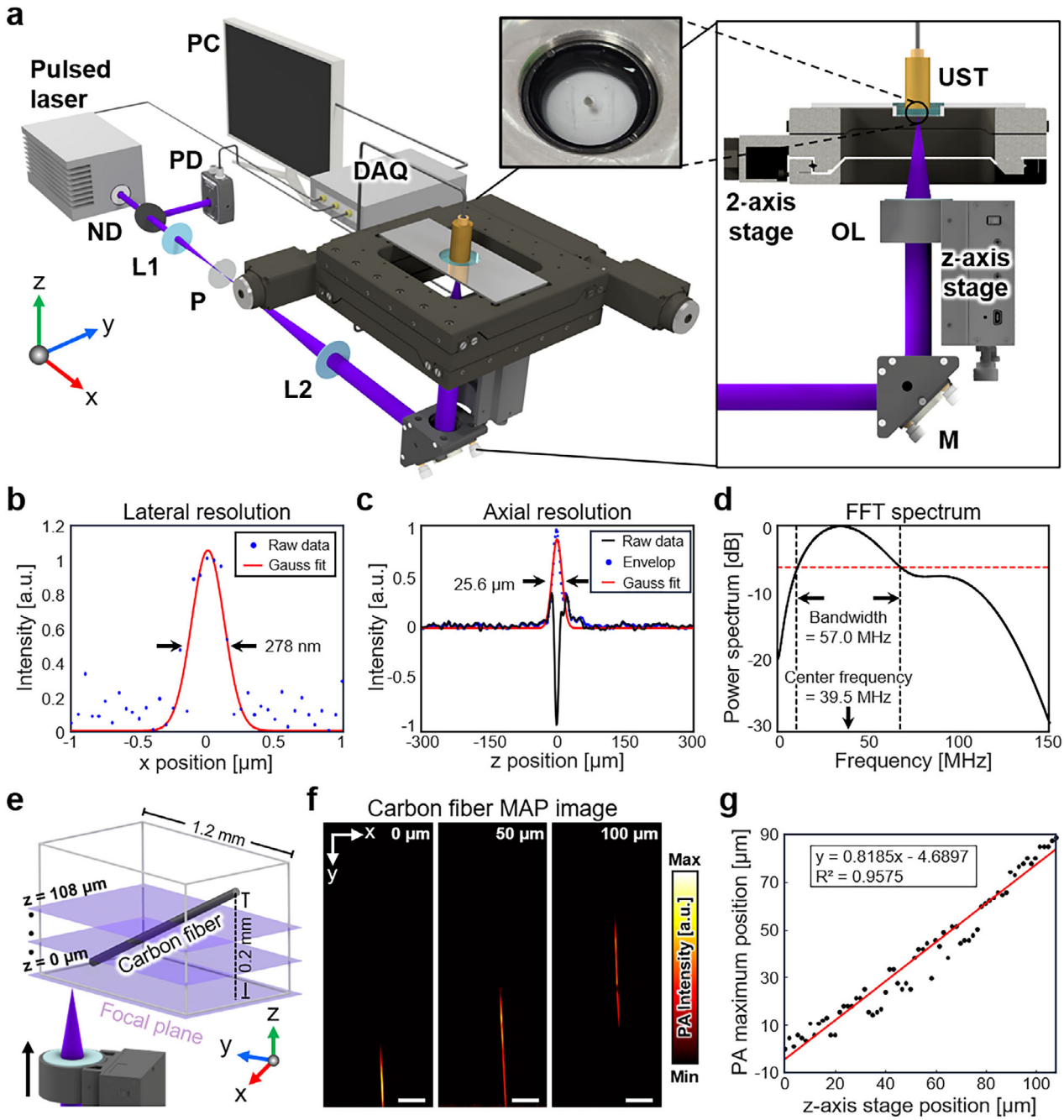

FIGURE 2 | Schematic of the UV-PAM-Z system and performance of the system, including resolution and z-axis scanning. (a) Schematic of the UV-PAM-Z system and enlarged view of the scanning region. The ND filter was used to control the laser power, while the PD was used to monitor the relative laser power. (b) Lateral resolution measurement using a 100 nm gold nanoparticle target. The measured intensity profile and corresponding Gaussian fit are shown. (c) Axial resolution measurement using an isolated carbon-fiber target suspended approximately 2 mm above the substrate. The acquired A-line signal, envelope signal, and corresponding Gaussian fit are shown. (d) Frequency spectrum of the PA signal generated from (c). (e) Schematic of the phantom used to validate the z-axis piezo stage, composed of an angled carbon fiber for depth-dependent imaging. (f) PA MAP images of the carbon fiber acquired at different z-stage positions (0, 50, and 100 μm; scale bar = 50 μm). (g) Linear correlation between the z-axis piezo stage position and the PA signal peak position, confirming accurate depth scanning performance. PC, personal computer; DAQ, digital acquisition; PD, photodetector; ND, neutral density filter; L, lens; P, pinhole; M, mirror; OL, objective lens; UST, ultrasound transducer; MAP, maximum amplitude projection; PA, photoacoustic; UV-PAM-Z, z-scanning UV photoacoustic microscopy; FWHM, full width at half maximum.

A total of 65 UV-PAM-Z volumetric datasets were acquired by scanning the z-axis in 1 V steps from 140 to 75 V, corresponding to approximately 108 μm in vertical displacement. Theoretically, the depth of field (DOF) of the transducer for PA signals is approximately 153 μm, which covers the entire 108 μm scanning range. Figure 2f shows representative PA maximum amplitude projection (MAP) images acquired at 140, 110, and 80 V applied to the piezo stage, corresponding to depths of 0, 50, and 100 μm from the quartz glass surface, respectively. These images show how the imaged region shifted upward as the focal plane moved

higher, reflecting consistent z-axis scanning. A full stack of 65 MAP images was analyzed to quantitatively validate the z-axis performance of the system. The axial positions of the maximum PA signals in each image were identified and used to calculate the corresponding focal positions, which were then compared with the known stage displacements. By tracking the axial position of the maximum signal along the image stack, we detected a strong linear relationship ($R^2 = 0.9575$) between the focal shift and stage displacement using linear regression analysis (Figure 2g). This confirms that the z-axis stage allows for accurate and linear depth control in PA imaging.

2.2 | Quantitative Validation of Nuclear Imaging in Organoid Slices

To validate the nuclear imaging capability of UV-PAM-Z, we compared its images with optical microscopy images of corresponding organoid sections. The cortical organoids used in this experiment were 95 days old. Organoid slices were first imaged in a label-free manner using UV-PAM-Z and subsequently stained with DAPI. Figure 3a–c shows the corresponding slice regions imaged using bright-field microscopy (BFM), FLM, and UV-PAM-Z, respectively. The BFM image and DAPI-stained FLM image were visualized using a 25× objective lens. For UV-PAM-Z, whole-slice imaging was performed with step sizes of 0.5 and 1.25 μm in the x and y directions, respectively. The yellow boxes in each image indicate the corresponding region, measuring 80 × 80 μm^2, which was magnified for detailed comparison. The BFM image shows the overall cellular morphology but does not allow for clear distinction of individual nuclei. In contrast, both the DAPI and UV-PAM-Z images distinctly visualize single-cell nuclei in the corresponding regions, indicating that UV-PAM-Z provides better contrast than BFM for identifying individual nuclei without labeling.

UV-PAM-Z was used to image a small 0.2 × 0.2 mm^2 region with finer step sizes of 0.5 and 0.625 μm in the x and y directions, respectively, allowing for precise quantitative analysis of cell nuclei. When comparing the signal-to-noise ratio (SNR) of the same nuclei imaged in the same region using DAPI fluorescence and UV-PAM-Z, the SNRs were 14.83 and 17.84 dB, respectively (Figure S3). This indicates that UV-PAM-Z provides more than 3 dB higher contrast than DAPI staining under identical imaging conditions. To allow for quantitative analysis of nuclear morphology, DAPI and UV-PAM-Z images were compared using the same field of view (FOV). Figure 3d,e show DAPI and UV-PAM-Z images from an identical FOV, with a consistent cell edge detection method applied to both modalities. Following the same procedure described above, the organoid section was first imaged using UV-PAM-Z and subsequently stained and imaged using DAPI fluorescence microscopy. A total of 534 and 485 nuclei were detected in the DAPI and UV-PAM-Z images, respectively, corresponding to a discrepancy of approximately 9.2%. Such a discrepancy may arise from sample mismatch introduced during the post-imaging processing steps required for DAPI staining, washing, and mounting (Figure S4). These procedures can introduce slight structural deformation, positional shifts, or partial loss of loosely attached tissue regions, which may complicate exact one-to-one correspondence between the UV-PAM-Z and DAPI images. Figure 3f shows histograms of nuclear counts by area and maximum diameter, derived from the edge detection results of both images. The DAPI and UV-PAM-Z histograms showed substantial overlap in both nuclear area and maximum diameter. The mean nuclear area was 14.08 ± 7.04 μm^2 for DAPI and 13.31 ± 6.80 μm^2 for UV-PAM-Z. The mean nuclear diameters were 5.54 ± 1.81 μm and 5.38 ± 1.79 μm, respectively. This indicates that UV-PAM-Z provides nuclear morphological information comparable to that obtained using DAPI.

To examine individual cell nuclei, the 25 × 25 μm^2 yellow boxes in Figure 3d,e were magnified and examined (Figure 3g,h). The intensity profiles in both images were extracted along the yellow lines that cross the two nuclei, as shown in Figure 3i. Pearson's linear correlation analysis yielded a coefficient of 0.843 between the two profiles. Despite the intermediate sample-processing steps, the overall nuclear boundaries remained highly consistent between the two imaging modalities. The two magnified images were overlaid, and the nuclei were highlighted with yellow ellipses (Figure 3j). The center positions of the six highlighted nuclei were mapped onto the x–y plane (Figure 3k). The average positional deviation was 0.86 ± 0.35 μm, reflecting high spatial agreement between UV-PAM-Z and DAPI images. This minor deviation may have resulted from sample alterations during the staining process. By eliminating the need for staining and other preparation steps, label-free UV-PAM-Z imaging preserves the native nuclear morphology. This enables more accurate morphological analysis and reliable interpretation of the cellular state.

2.3 | Label-Free z-Scanned Nuclear Imaging of Intact Live Organoids

To evaluate the intact live organoid imaging capability of the UV-PAM-Z system, label-free imaging was performed on live 96-day-old cortical organoids without staining or sectioning. The organoid, approximately 2 mm in diameter, was mounted onto a 3D-printed ethanol-sterilized holder with an approximately 2.4 mm inner hole (the left panel of Figure 4a). A wide-field UV-PAM-Z image (the right panel of Figure 4a) covering a 2.5 × 2.5 mm^2 area was acquired from the identical specimen previously observed under a photo. To assess spatial uniformity within the organoid, the central surface region highlighted by the yellow box in the right panel of Figure 4a was selected. This region, measuring 0.9 × 0.9 mm^2, was enlarged for detailed analysis (Figure 4b). This region was then divided into a 3 × 3 grid, yielding nine subregions of 0.3 × 0.3 mm^2 each for quantitative analysis. Prior to nuclear quantitative analysis, we examined the corresponding xz projection image of the region used for MAP-based nuclear analysis to evaluate the extent of potential depth overlap within the analyzed ROI (Figure S5). Laser excitation was delivered through the bottom surface of the quartz substrate. Therefore, the lower boundary of each nuclear PA signal corresponded to the region of the nucleus closest to the substrate. Representative nuclear PA signals were observed within an axial range of approximately 1–12 μm above the substrate, indicating that the analyzed ROI was effectively quasi-2D with only limited axial overlap between neighboring nuclei. Therefore, the generated MAP images primarily represented individual nuclei rather than extensive superposition of nuclei distributed across multiple depth layers for quantitative analysis.

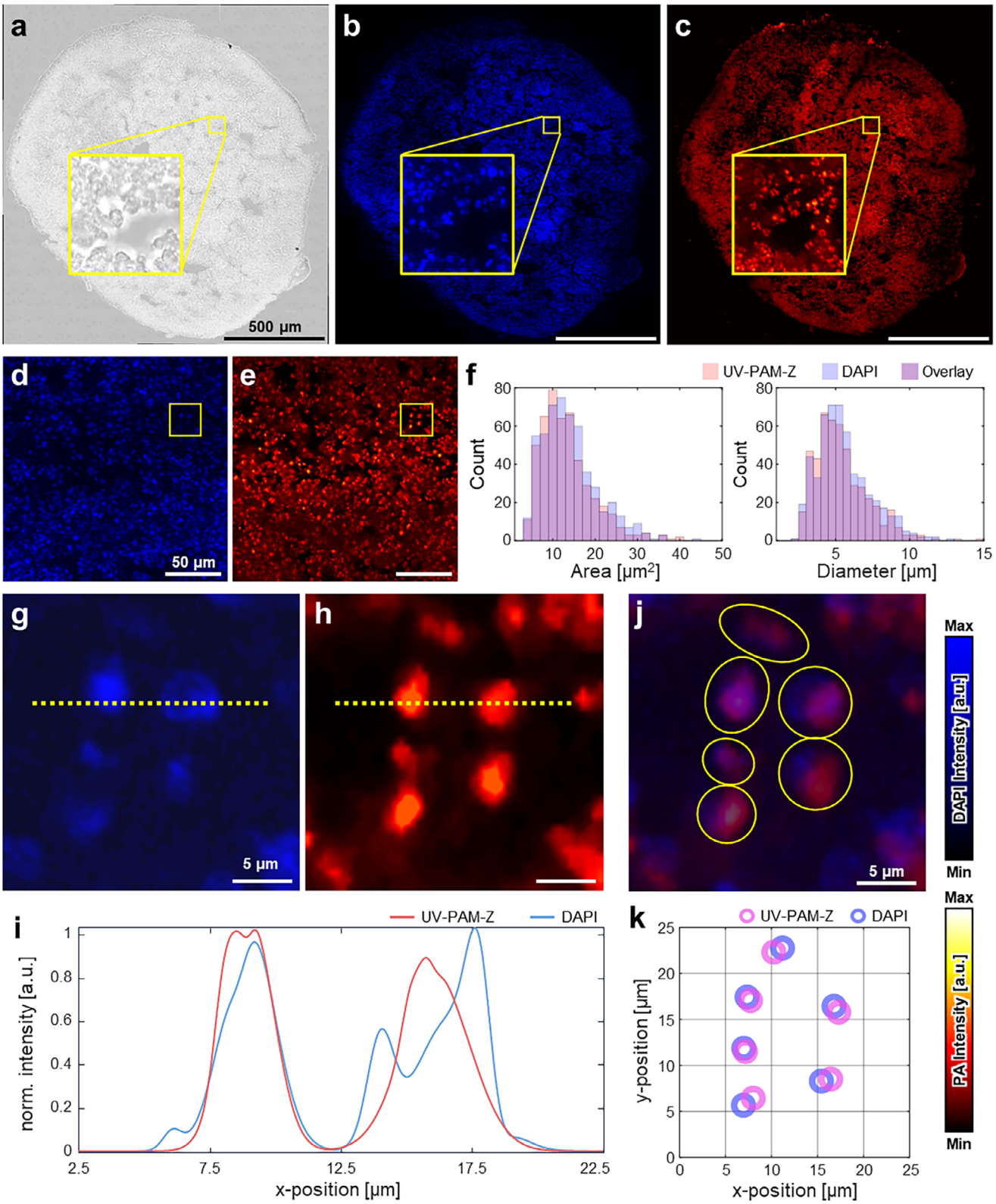

FIGURE 3 | Validation of UV-PAM-Z system reliability by quantitative comparison with DAPI-stained nuclear imaging. (a–c) Brightfield, DAPI, and UV-PAM-Z images of the same organoid section region. The UV-PAM-Z image was acquired prior to staining. (d,e) DAPI and high-precision step-size UV-PAM-Z images in the same region. (f) Histograms of nuclear area and maximum diameter analyzed from images in (d,e). (g,h) Magnified DAPI and UV-PAM-Z images of the yellow boxed regions in (d,e), respectively. (i) Normalized intensity profiles along the yellow lines in (g,h). (j) Overlayed image of (g,h), showing co-registered nuclear signals from UV-PAM-Z and DAPI in the same location. (k) Spatial centroid positions of corresponding nuclei from UV-PAM-Z and DAPI images. UV-PAM-Z, z-scanning UV photoacoustic microscopy; norm, normalized.

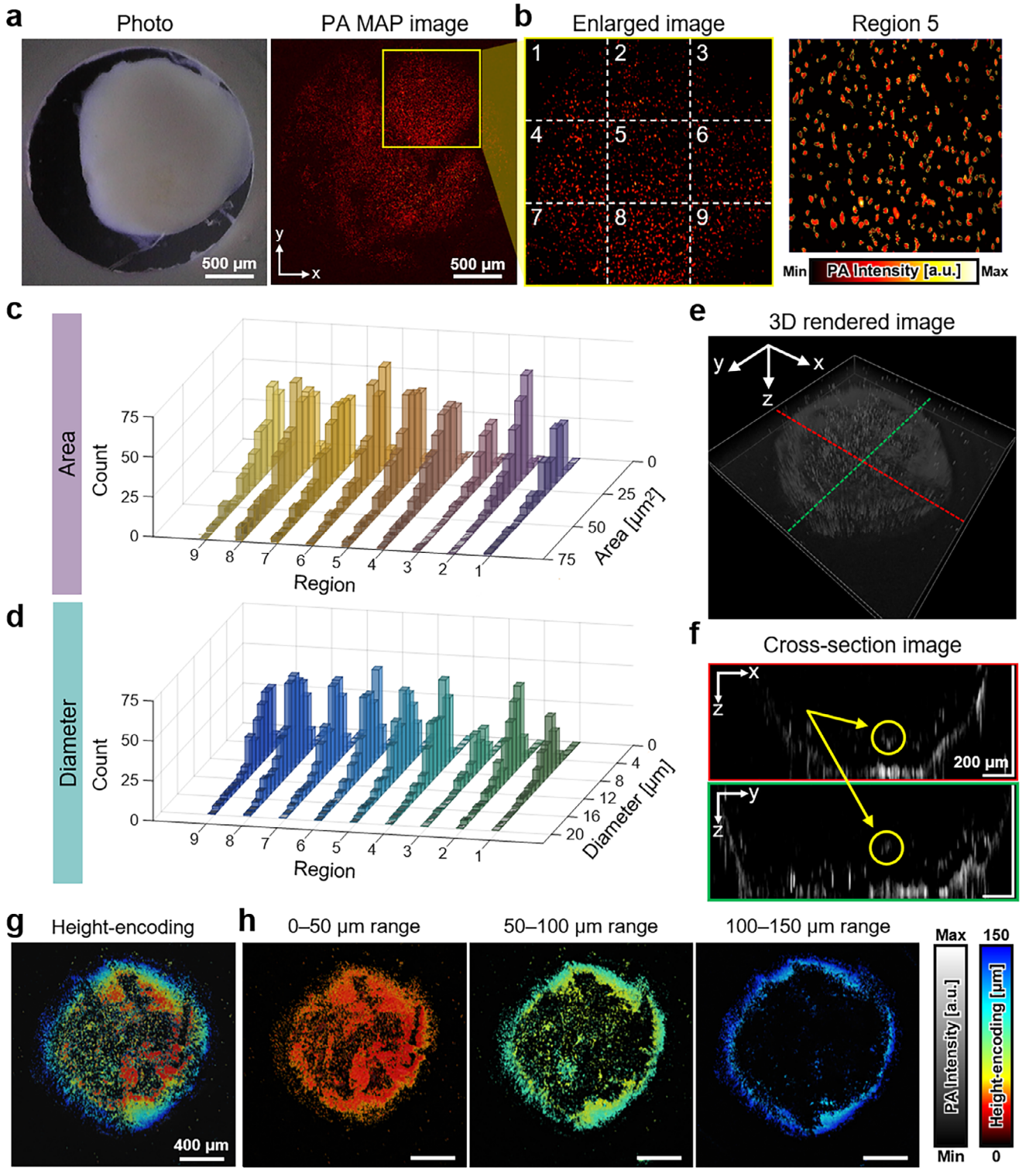

FIGURE 4 | Intact organoid imaging and 3D visualization using UV-PAM-Z. (a) Macroscopic image of the organoid and corresponding intact organoid PA MAP image acquired with UV-PAM-Z. (b) Enlarged image (yellow box), showing segmented grid (3 × 3) and individual nucleus-level visualization. Edge-detected result of a representative region selected from the enlarged image. (c) 3D histogram showing the regional distribution of nuclear area quantified from the nine segmented regions. (d) 3D histogram showing the regional distribution of nuclear diameter quantified from the nine segmented regions. (e) 3D-rendered image of the entire organoid reconstructed from three z-stack images. (f) Orthogonal cross-sectional B-mode images extracted from the dataset shown in (e): xz plane (top, along the red line) and yz plane (bottom, along the green line). Representative nuclear PA signals are highlighted by yellow circles. (g) Height-encoded MAP image representing the height distribution of nuclei, derived from (e). (h) Height-resolved images obtained by stepwise slicing from the bottom surface in 50 μm intervals. PA, photoacoustic; MAP, maximum amplitude projection; UV-PAM-Z, z-scanning UV photoacoustic microscopy.

The right panel of Figure 4b shows the edge detection results for the central subregion (Region 5). Figure 4c,d show 3D histograms representing the distribution of these metrics. A total of 2,095 nuclei were detected across the full 0.9 × 0.9 mm^2 region. The average total nuclear area and diameter were 27.42 ± 15.39 μm^2 and 8.52 ± 4.24 μm, respectively. The nuclear morphology of each of the nine subregions was analyzed independently (Table S1). To determine the representativeness of the localized measurements, we calculated the mean and standard deviation for each subregion before averaging them across all nine regions. The resulting values were 26.33 ± 14.03 μm^2 for nuclear area and 8.34 ± 3.51 μm for diameter, closely matching the full-area averages. Despite the measured dispersion in nuclear size, the distribution of nuclear features was consistent across spatial regions, indicating spatial uniformity in nuclear morphology throughout the organoid [37].

To verify the 3D imaging performance of the system, the intact organoid sample was imaged at three different focal positions through z-axis stage translation. The piezo stage was incrementally shifted upward in 50 μm steps from the top surface of the quartz glass. An FOV of 2 × 2 mm^2 was scanned with lateral step sizes of 0.5 and 1.25 μm, and the acquired data were reconstructed into a 3D rendered image (Figure 4e and Movie S1). Cross-sectional images along both the x- and y-axes (corresponding to the red and green lines in Figure 4e, respectively) revealed the organoid's spherical morphology and detectable signals up to approximately 180 μm above the quartz glass surface (Figure 4f). Additionally, as indicated by the yellow arrows and circular markers, nuclear PA signals were detected at depths of approximately 57.3 and 67.3 μm in the xz and yz planes, respectively. Figure 4g shows height-encoded projections of the entire volume. Height encoding was referenced to the organoid surface, allowing for visualization of the vertical distribution of nuclear PA signals. The imaging volume was segmented into discrete depth intervals relative to the organoid surface (0–50 μm, 50–100 μm, and 100–150 μm) to improve visualization of nuclear distribution across different depths (Figure 4h). Nuclear signals were distinctly observed in the superficial (0–50 μm) and intermediate (50–100 μm) layers. However, beyond 100 μm, the PA signal intensity decreased significantly, particularly in the central area of the organoid. These findings demonstrate that the UV-PAM-Z system allows for high-resolution, depth-resolved imaging of subvolumes within intact live organoids down to a depth of 100 μm without sectioning the sample.

The biological impact of UV exposure under the UV-PAM-Z imaging conditions was further assessed using additional Live/Dead and MTT assays (Figure S6). Five control organoids and five UV-exposed organoids were analyzed for each assay. For the UV-exposed group, organoids were scanned using the same imaging conditions employed throughout this study (laser power: 0.3 mW; step sizes: x = 0.2 μm, y = 0.625 μm) over a 1.5 × 1.5 mm^2 area, covering most of the organoid surface. Following UV exposure, organoids were allowed to recover for 2 h prior to viability assessment. Live/Dead staining revealed a lower mean viability in the UV-exposed group (59%) than in the control group (73%), although the difference was not statistically significant (p = 0.2303). Similarly, MTT analysis showed that UV-exposed organoids retained 97% of the metabolic activity observed in the control group, with no statistically significant difference between groups (p = 0.6056). Given the strong absorption of 266 nm UV light by nucleic acids, some degree of UV-induced cellular stress is biologically plausible and cannot be completely excluded. However, under the imaging conditions used in this study, neither the Live/Dead assay nor the MTT assay provided evidence of substantial organoid-level toxicity.

2.4 | Label-Free Imaging and Analysis of EtOH-Induced Nuclear Alterations

Prenatal or chronic EtOH exposure has been implicated in various neurodevelopmental and neurodegenerative disorders, including FASDs, owing to its disruptive effects on neural proliferation, migration, and tissue architecture [1–4]. To model these pathological conditions in a human-relevant system, we used 3D cortical organoids and exposed them to 2% (v/v) EtOH. This acute challenge model was designed to induce measurable structural damage in a controlled environment, allowing for the assessment of EtOH-induced nuclear alterations using label-free high-resolution UV-PAM-Z imaging. For UV-PAM-Z imaging, organoids were divided into two groups: a control group without treatment and an EtOH-treated group exposed to 2% (v/v) EtOH for 6 h. To quantitatively evaluate nuclear morphology in response to treatment, seven organoids per group were used as biological replicates, and the central region of each organoid was imaged. Distinct color maps were used to differentiate the control and EtOH-treated groups for visualization. In Figure 5a, individual nuclei from three representative organoids were clearly visualized within an FOV measuring 0.1 × 0.1 mm^2, acquired with step sizes of 0.25 and 0.625 μm along the x- and y-axes, respectively. Notable morphological differences in the individual nuclei were observed between the control (I–III) and EtOH-treated (IV–VI) groups. The nuclei in the EtOH-treated samples exhibited more structural irregularities, including deformation and fragmentation, than the relatively uniform nuclei in the control group. These morphological alterations were consistently observed in the treated samples. These changes suggest that EtOH exposure causes nuclear damage or cellular stress responses. For detailed visual comparison, representative nuclei (CTL and i–iv) from each group were enlarged to 10 × 10 μm^2 (Figure 5b). The magnified images revealed distinct morphological differences. Nuclei in the control group (CTL) maintained a smooth, intact structure. In contrast, the EtOH-treated nuclei (i–iv) showed significant size reductions and clear signs of fragmentation, with split or irregularly shaped subregions, indicating possible nuclear disassembly. These findings show that UV-PAM-Z imaging enables the visualization of EtOH-induced morphological alterations in cell nuclei.

Subsequently, edge detection was applied to a total of 625 nuclei identified in fourteen organoids, including 239 nuclei from seven control organoids and 386 nuclei from seven EtOH-treated organoids, allowing statistical quantification of morphological changes. Three morphological parameters were quantified across the two groups, and to perform comparisons at the organoid level, the mean value from each organoid was calculated prior to statistical analysis using a two-tailed unpaired t-test (Figure 5c). The EtOH-treated group had a smaller average nuclear area (22.87 ± 5.24 μm^2) compared to the control group (42.46 ± 3.98

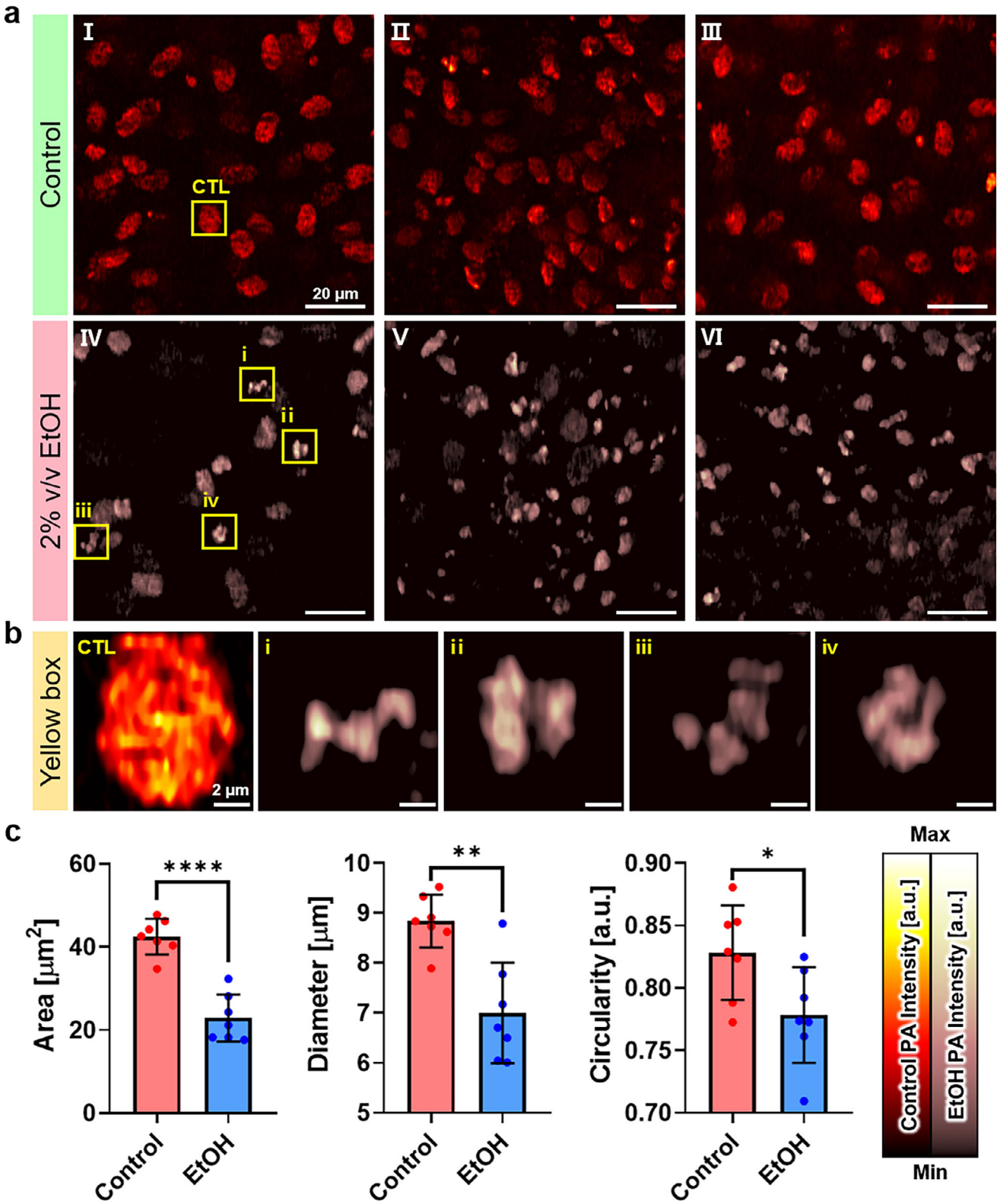

FIGURE 5 | Comparison of morphological changes and statistical analysis of nuclei in organoids following control and alcoholic challenge. (a) Representative UV-PAM-Z MAP images of nuclei from control (I–III) and EtOH-treated (IV–VI) organoids. (b) Enlarged nuclear morphologies extracted from selected yellow boxes in a (CTL, i–iv). (c) Bar graphs with scatter overlay showing the statistical distributions of nuclear area, maximum diameter, and circularity for control and EtOH-treated groups. Each data point represents one organoid ($n = 14$ total organoids; $n = 7$ per group). (*, $p < 0.05$; **, $p < 0.01$; ****, $p < 0.0001$; unpaired t-test). CTL, control; PA, photoacoustic; EtOH, ethanol; UV-PAM-Z, z-scanning UV photoacoustic microscopy; MAP, maximum amplitude projection.

μm^2), which was statistically significant ($p < 0.0001$). Similarly, the average maximum caliper diameter was significantly lower in the EtOH-treated group (7.00 ± 0.93 μm) compared to the control group (8.84 ± 0.49 μm; $p = 0.0011$). Although the difference in average circularity between the control (0.83 ± 0.04) and EtOH-treated (0.78 ± 0.04) groups was smaller than that observed for area and diameter, it was still statistically significant ($p = 0.0307$). To complement the group-level statistical analysis, we selectively compared four morphologically intact and four severely disrupted nuclei, which represented the most extreme cases observed in the dataset (Figure S7). This targeted comparison revealed more pronounced differences, with nuclear area and diameter decreasing by 55.7% and 31.3%, respectively, while circularity decreased by 3.5% [38]. To evaluate inter-organoid variability among control samples, nuclear morphology parameters were additionally compared across seven independent control organoids using one-way ANOVA followed by Tukey's post hoc test (Figure S8). For nuclear area, statistically significant differences were observed only between organoids #2 and #3 ($p = 0.0170$) and between organoids #3 and #5 ($p = 0.0327$) (Figure S8a). Similarly, for nuclear diameter, statistically significant differences were observed only between organoids #2 and #3 ($p = 0.0049$) and between organoids #3 and #5 ($p = 0.0124$) (Figure S8b). For nuclear circularity, statistically significant differences were observed only between organoids #2 and #6 ($p = 0.0203$) and between organoids #4 and #6 ($p = 0.0128$) (Figure S8c). Although a limited number of pairwise differences reached statistical significance among independent control organoids, most comparisons were not statistically significant across all three nuclear morphology parameters. These findings indicate that nuclear morphology parameters were generally consistent across independent control organoids and exhibited only limited inter-organoid variability.

To further support the biological relevance of the nuclear alterations detected by UV-PAM-Z, additional fluorescence staining experiments were performed under the same treatment conditions using cleaved caspase-3 (cCas-3), γ-H2AX, and TUNEL (Figure S9). Representative fluorescence images showed visibly stronger cCas-3, γ-H2AX, and TUNEL signals in EtOH-treated organoids compared with controls. Quantitative analysis further confirmed significant increases in cCas-3 ($p = 0.0079$), γ-H2AX ($p = 0.0079$), and TUNEL ($p = 0.0317$) signals following EtOH treatment. These findings indicate that the nuclear shrinkage and fragmentation observed by UV-PAM-Z are associated with EtOH-induced apoptotic processes.

2.5 | Machine Learning-Based Classification of EtOH-Induced Nuclear Alterations

To assess the feasibility of UV-PAM-Z as a label-free drug screening platform, we performed a proof-of-concept machine learning-based classification of EtOH-induced nuclear alterations using quantitative nuclear morphological features extracted from UV-PAM-Z images (Figure 6). A total of 625 nuclei were included in the analysis, comprising 239 control nuclei and 386 EtOH-treated nuclei obtained from seven control and seven EtOH-treated organoids. A linear support vector machine (SVM) classifier was employed for classification analysis. To minimize potential data leakage, the dataset was divided at the organoid level rather than the nucleus level using a leave-one-organoid-pair-out cross-validation strategy. In each of the seven cross-validation iterations, one control organoid and one EtOH-treated organoid were held out for testing, while the remaining six organoid pairs were used for training. Consequently, nuclei originating from a given organoid were exclusively assigned to either the training or testing set and were never shared between the two datasets during model evaluation. The mean and standard deviation of accuracy, sensitivity, specificity, and area under the receiver operating characteristic (ROC) curve (AUC) were calculated across all iterations. In this analysis, 2D feature spaces were used to evaluate separability at the level of individual nuclear morphological descriptors, whereas 3D feature integration was employed to assess EtOH-induced nuclear phenotypes at a multivariate level. In addition, the pooled ROC curves shown in Figure 6 were generated by aggregating prediction results obtained exclusively from unseen test organoids across all leave-one-organoid-pair-out cross-validation iterations. Consequently, the reported ROC curves reflect classification performance on independently evaluated organoids without nucleus-level train-test mixing.

We first evaluated classification performance in 2D feature spaces to determine whether individual nuclear morphological descriptors provide sufficient separability between control and EtOH-treated nuclei. Specifically, area-diameter and area-circularity feature pairs were examined to assess whether EtOH-induced nuclear alterations manifest as distinct phenotypes along nuclear size- and shape-related axes (Figure 6a). In both feature spaces, EtOH-treated nuclei exhibited a systematic shift toward lower area, diameter, and circularity values compared with control nuclei, although partial overlap between the two groups was observed. Using a linear SVM, classification in the area-diameter feature space yielded a mean AUC of 0.86 ± 0.06 (pooled AUC = 0.88), with a mean accuracy of 82.2% ± 10.9% (sensitivity = 84.5% ± 12.6%, specificity = 75.7% ± 11.4%) for detecting EtOH-treated nuclei. Similarly, classification in the area-circularity feature space achieved a mean AUC of 0.86 ± 0.09 (pooled AUC = 0.89), with a mean accuracy of 83.2% ± 9.7% (sensitivity = 83.5% ± 14.6%, specificity = 77.9% ± 9.4%). These results indicate that individual nuclear morphological descriptors derived from UV-PAM-Z images capture biologically meaningful signatures of EtOH-induced nuclear alteration at the feature level.

While individual morphological features provide meaningful separability, drug-induced nuclear phenotypes are inherently multivariate, reflecting concurrent changes in nuclear size and shape. To evaluate whether EtOH-induced nuclear alterations are more robustly captured when multiple descriptors are jointly considered, we extended the analysis to a 3D feature space integrating nuclear area, diameter, and circularity (Figure 6b).

In the 3D feature space, ROC analysis yielded a mean AUC of 0.85 ± 0.08 (pooled AUC = 0.87), and the classifier achieved a mean accuracy of 83.6% ± 8.8%, with a sensitivity of 85.8% ± 13.3% and a specificity of 75.3% ± 11.0%. Overall, comparable classification performance was maintained across all feature combinations under the organoid-level validation framework, with all models achieving mean AUC values above 0.85. These results indicate that quantitative nuclear morphological features extracted from UV-PAM-Z images can robustly distinguish EtOH-treated nuclei from control nuclei. These results demonstrate that

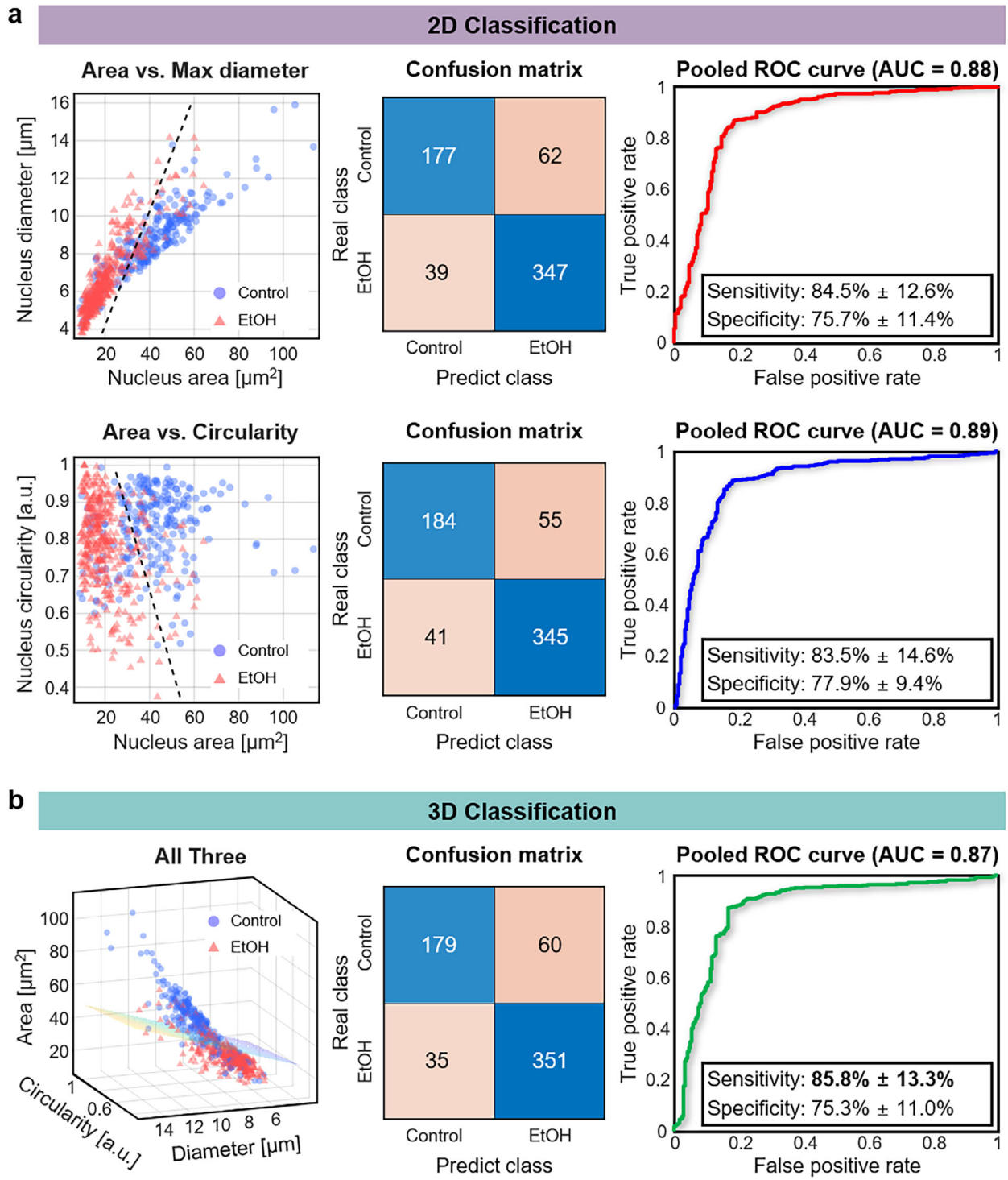

FIGURE 6 | Machine learning-based classification of control and ethanol-treated nuclei using nuclear morphological features. (a) 2D feature space-based classification using area-diameter and area-circularity feature pairs (left: scatter plot, middle: confusion matrix, right: ROC curve). (b) 3D feature space-based classification integrating area, diameter, and circularity. The displayed scatter plots, confusion matrices, and ROC curves represent pooled results obtained from seven iterations of leave-one-organoid-pair-out cross-validation.

nuclear morphology derived from UV-PAM-Z images encodes drug-induced phenotypic signatures at the single-nucleus level. By enabling both feature-level interrogation of individual morphological descriptors and phenotype-level integration through multivariate analysis, UV-PAM-Z provides a label-free platform capable of quantitatively screening drug-induced nuclear responses without reliance on exogenous staining or molecular labeling.

3 | Discussion and Conclusion

Recent advances in organoid technology have established 3D models as effective platforms for studying human brain development, disease mechanisms, and drug responses. Among various disorders, FASD is of particular importance because of the high prevalence of prenatal EtOH exposure, which causes disrupted neurogenesis, increased apoptosis, and long-term cognitive deficits [2, 5]. These abnormalities can be evaluated at the cellular level based on changes in nuclear morphology, which is a sensitive marker of early-stage cytotoxicity. However, conventional FLM, such as immunostaining and DAPI labeling, requires fixation, staining, and physical sectioning, which are time-consuming and frequently introduce structural artifacts into thick 3D organoid samples. Moreover, long-term monitoring is hindered by photobleaching and phototoxicity, highlighting the need for improved label-free imaging approaches [20, 21].

In this study, we developed and applied UV-PAM-Z to intact live cortical organoids and achieved sub-micrometer resolution sufficient to resolve individual nuclei, including fragmented nuclei that are commonly observed under cytotoxic stress. Nuclear visualization was possible using volumetric scanning on samples with a 2 mm diameter and depths exceeding 100 μm. In EtOH-treated organoids, nuclear area, diameter, and circularity decreased by 46.1%, 20.8%, and 6.0%, respectively, compared to controls, demonstrating significant cytotoxicity. Furthermore, a linear SVM classifier trained on these morphological features achieved organoid-level cross-validation mean accuracies of 82.2%–83.6% with AUC values of 0.85–0.86, underscoring the potential of UV-PAM-Z as a proof-of-concept platform for automated drug-response evaluation based on label-free nuclear morphological analysis in intact organoids. Cytotoxic stress induces nuclear fragmentation, producing structures smaller than typical nuclei, which our UV-PAM-Z system could clearly resolve in intact cortical organoids. Using this label-free approach, we observed significant reductions in nuclear area under EtOH treatment, consistent with cytotoxic damage. Therefore, the ability to resolve fragmented and size-reduced nuclei under cytotoxic stress highlights the biological relevance of UV-PAM-Z for accurately capturing nuclear alterations that underlie neurotoxicity.

In densely populated 3D tissues, MAP processing may merge signals originating from nuclei located at different depths, potentially affecting the measured nuclear size or shape. However, the analysis performed in this study was not intended as a complete census of all nuclei throughout the entire organoid volume. Rather, it was designed to compare nuclear morphological changes within a selected ROI under identical imaging and analysis conditions. The ROI used for nuclear morphology analysis was defined within a superficial region of the organoid. Therefore, the reported results should be interpreted as a comparative assessment of nuclear morphology within the analyzed ROI rather than a comprehensive characterization of all nuclei throughout the entire organoid volume. Furthermore, both control and EtOH-treated organoids used the identical acquisition and analysis workflow. Even if a limited degree of projection-related distortion were present, it would be expected to affect both groups similarly and is unlikely to account for the observed differences in nuclear morphology. Additional segmentation validation analyses indicated that the reported morphological trends were robust and were not driven by specific segmentation or image-processing parameters. Nevertheless, MAP-based analysis may still be affected by partial depth-overlap artifacts in highly dense tissues. Future improvements in axial resolution and depth-resolved image reconstruction may enable more accurate 3D nuclear morphology quantification.

Despite the advances demonstrated in this study, UV-PAM-Z still has several limitations. Under the current system configuration, a representative FOV for drug evaluation required approximately 30 s for image acquisition. Imaging-speed optimization further reduced the acquisition time to approximately 15 s while preserving reliable nuclear morphology information, and individual nuclei remained distinguishable even at acquisition times of approximately 8 s (Figure S10; see Methods for detailed acquisition parameters). Nevertheless, current imaging speed is restricted by the reliance on mechanical scanning, which affects the feasibility of imaging under live conditions. Incorporating galvo-based laser scanning could substantially accelerate data collection and help overcome this limitation [39, 40]. In addition, the integration of MEMS scanners and polygon mirrors may enable further system miniaturization and real-time imaging capabilities [30, 41, 42]. Such optical scanning approaches are expected to substantially improve imaging throughput by eliminating the need for mechanical stage movement. In addition, further improvements in imaging speed may be achieved through the use of higher laser pulse repetition rates. The short DOF inherent to high-resolution optics constrains volumetric coverage and requires frequent refocusing. Although z-scanning was employed to partially compensate for the restricted DOF, optical attenuation and scattering at UV wavelengths continue to limit the visualization of nuclei in deeper regions of large intact organoids. Consequently, the current approach may underestimate the total nuclear population in these regions and is not intended for absolute whole-organoid nuclear quantification. Instead, the present analysis focuses on ROI-based evaluation of nuclear morphology and spatial distribution within regions that can be reliably visualized under the current imaging conditions. Within this framework, the proposed approach enables quantitative comparison of nuclear morphological changes and cytotoxic responses between experimental groups acquired under identical imaging conditions. In future studies, advanced optical designs such as extended DOF systems (e.g., metalenses) and AI-based reconstruction could further reduce distortion and extend effective imaging depth [20, 22, 34, 43–45]. Metalenses, with their engineered phase profiles, may help compensate for uneven sample surface topography while preserving resolution. Meanwhile, AI-based reconstruction can algorithmically restore defocused features, effectively expanding usable depth and minimizing the need for repeated mechanical refocusing. An additional consideration of the proposed approach is the potential biological impact of 266 nm UV excitation. In this regard, Live/Dead and MTT assays revealed no statistically significant changes in organoid-level viability or metabolic activity following UV-PAM-Z imaging, although a reduction in mean viability was observed in the Live/Dead assay. This apparent discrepancy may arise because organoid-level viability assays can underestimate localized surface-level effects confined to the superficial UV-exposed region. Importantly, the objective of the present work

was to characterize drug-induced nuclear morphological alterations at a predefined experimental endpoint rather than to evaluate post-imaging organoid viability or long-term biological responses following UV exposure. Therefore, although localized UV-induced effects may occur, the proposed approach remains suitable for comparative assessment of drug-induced nuclear morphological alterations in intact organoids at a predefined endpoint. In this study, the imaging conditions were selected to provide sufficient nuclear contrast and image quality for reliable quantitative assessment of nuclear morphology, rather than to minimize the excitation energy to the lowest achievable level (Figure S11; see Methods for details). Although careful fluence adjustment and faster scanning can reduce cumulative exposure, these strategies may only minimize rather than eliminate this risk [46, 47]. Future developments in alternative excitation schemes or advanced detection methods could further expand their applicability to live or longitudinal imaging. As a proof-of-concept study, the current work was limited to a single organoid model and treatment conditions. Validation across larger biological cohorts, diverse organoid systems, patient-derived organoids, and additional drug conditions will be necessary to establish the robustness, broader applicability, and utility of the proposed approach for organoid-based drug evaluation and screening.

In conclusion, UV-PAM-Z provides unique advantages for high-resolution, label-free nuclear imaging of intact organoids. This system minimizes structural distortion while preserving native cellular states by allowing intact organoid visualization without staining or sectioning. Although challenges remain, our findings show that UV-PAM-Z allows for more accurate assessment of nuclear morphology and cytotoxic changes. With further technical refinements, this approach has the potential for broad use in organoid-based disease modeling, high-content drug screening, and translational research.

4 | Experimental Section

4.1 | Maintenance and Subculture of hiPSCs

To culture a commercial hiPSC cell line (E3/E4, BIONi010-C; from the European Bank for Induced Pluripotent Stem Cells), 100 mm culture plates were coated with 5 mL of ESC-qualified Matrigel (Corning Matrigel hESC-Qualified Matrix, #354277, Corning, USA) in DMEM/F-12 with GlutaMAX (10565-018, Gibco, USA) coating solution per plate. The plates were then incubated at room temperature for 1 h. Passaging occurred when hiPSC confluency exceeded 70%. Following the removal of the medium from the hiPSC plates, the cells were washed with DPBS. Four milliliters of non-enzymatic passaging solution ReLeSR (ST05872, StemCell Technologies, Canada) was added. After approximately 30 s at room temperature, most of the ReLeSR was removed, leaving a thin layer. The plate was incubated for 5 min at room temperature, followed by another 2 min in a 37°C, 5% CO_2 incubator. Following incubation, the remaining ReLeSR was removed, and 4 mL of mTeSR + was added to collect the detached colonies in a 15 mL conical tube. The cells were centrifuged at 300 × g for 2 min at room temperature. After removing the supernatant, 3 mL of mTeSR medium was added to resuspend the cells. Finally, 300 µL of the suspension was plated onto a new culture plate, spread evenly, and incubated at 37°C with 5% CO_2. After 1 day of subculture, the plate was washed with 7 mL of Dulbecco's phosphate-buffered saline (DPBS, 14190-146; Gibco, USA), and the mTeSR + medium (ST100-0276, Stemcell Technologies, Canada) was changed. The medium was changed every day until the confluence reached more than 70% of the 100 mm cell culture plate. The detailed procedures were described in a previous study [14].

4.2 | Generation of hiPSC-Derived Cortical Organoid

The process of generating cortical organoids was described in a previous study [14]. Briefly, the process started on day 0, when the cells were seeded onto an AggreWell plate. EB medium was used to form EB from days 0 to 1. From days 2 to 5, dorsomorphin was added to block the bone morphogenetic protein pathway, while SB431542 was added to inhibit the transforming growth factor beta, Activin, and Nodal pathways. This prevented hiPSCs from differentiating into endoderm or mesoderm, directing them toward the neuroectoderm lineage. On day 6, the organoids were collected in a 100 mm Petri dish and shaken using an orbital shaker in an incubator with neuronal differentiation medium. On day 7, the cortical organoids were transferred to 96-well ultra-low-attachment U-bottom plates. From days 7 to 24, during the neuronal differentiation stage, epidermal and fibroblast growth factor were added to promote neural progenitor cell proliferation and differentiation into neuronal cells. From days 25 to 43, during the neuronal maturation stage, brain-derived neurotrophic factor and neurotrophin-3 were added to promote the growth of axons and dendrites in mature neurons, allowing the formation of neuronal networks and functional connections between different subtypes of neurons. Following maturation, brain organoids were cultured in conditioned basal medium to maintain their structure and function while shaking on an orbital shaker in an incubator.

4.3 | Cryosection and DAPI Staining

The obtained cortical organoid samples were washed three times with sterile PBS before being fixed in 4% paraformaldehyde (PC2031, SeorinBio, Korea) in DPBS for 24 h. After fixation, the organoids were washed three more times with DPBS and dehydrated in a 30% sucrose solution in distilled water for 72 h. Immediately after dehydration, the organoids were placed in the center of a mold with O.C.T compound FSC22 (3801480, Leica, Germany) and frozen at −80°C for storage. The frozen samples were sliced into 25 µm sections using a cryotome and then carefully placed on slide glasses.

Following cryosectioning, the samples were washed twice with sterile DPBS for 5 min each. They were then permeabilized for 20 min using 0.3% Triton X-100 (X100-5 mL, Sigma-Aldrich, Germany) in PBS (PBST) solution. After removing the PBST, a staining solution was prepared by mixing 4′,6-diamidino-2-phenylindole (DAPI) (D9542, Sigma-Aldrich, Germany) with distilled water in a 1:5000 ratio, and the samples were treated with this solution for 5 min. The DAPI staining solution was then removed, and the samples were washed twice with PBS for 5 min each. After drying, a mounting solution was used to mount the slides and prepare them for fluorescent imaging.

4.4 | Ultraviolet Photoacoustic Microscopy System

In the UV-PAM-Z system, a pulsed laser (DX-266-0.05, Photonics Industries, USA) operating at a wavelength of 266 nm was used for excitation. The laser beam was emitted with a pulse repetition rate of 20 kHz and a maximum output power of 50 mW. To eliminate the laser's residual 532 nm guide beam, a bandpass glass filter (FGUV5, Thorlabs, USA) was inserted into the optical path. The laser power was adjusted using a neutral-density filter (NDC-50C-4 M, Thorlabs, USA), and the reflected beam was collected using a photodetector (PDA10A2, Thorlabs, USA). To maintain a clean single-mode Gaussian beam profile, the beam was passed through a 10 μm diameter pinhole (84-909, Edmund Optics, USA). Two planoconvex lenses (LA4052-UV and LA4102-UV, Thorlabs, USA) were placed before and after the pinhole to focus and expand the beam. An iris diaphragm (SM1D25, Thorlabs, USA) was used to block the peripheral beam components and reduce the Airy disk's diffraction artifacts. The cleaned and collimated beams were reflected vertically using two UV-enhanced mirrors (PF20-03-F01, Thorlabs, USA) and focused onto the sample using an aspherical objective lens (AFL25-17-P-X, Asphericon, Germany) with a numerical aperture (NA) of 0.64 at 355 nm. We performed ZEMAX simulations to evaluate the chromatic focal shift over the wavelength range of 266–355 nm under the experimental conditions. The simulation results showed a wavelength-dependent focal shift across this wavelength range (Figure S12). Relative to the focal length at 355 nm (f = 10.00 mm), the focal length at 266 nm was calculated to be 9.329 mm, corresponding to a focal shift of 0.671 mm. The focus was adjusted along the z-axis using a motorized translation stage (CT1P/M, Thorlabs, USA) with a minimum step resolution of 0.5 μm. PA signals generated from the sample were detected using a single-element transducer (HFM23, Sonaxis, France) with a center frequency of 50 MHz, focal length of 3 mm, and 90% bandwidth. To ensure coaxial detection, the optical focus of the UV laser was aligned with the acoustic focus of the ultrasound transducer. The acquired signals were amplified to 48 dB using an amplifier (DPR500, JSR Ultrasonics, USA) and further processed using a hardware bandpass filter (3–150 MHz). For stable mounting and imaging of organoids, we used a custom-designed aluminum sample holder that accommodates 0.2 mm-thick quartz glass.

The entire scanning system was controlled using LabVIEW software (LabVIEW 2021, National Instruments, USA). Two-axis motorized stages (8MTF-75L-S05, Standa, Lithuania) were used for sample translation during scanning. The amplified PA signals were acquired using a digitizer (ATS9352, Alazartech, Canada) with a maximum sampling rate of 500 MS/s. The pulsed-laser trigger, motorized stage control, and digitizer acquisition trigger were all synchronized using a multichannel I/O device (NI-PCIe-6361, National Instruments, USA).

4.5 | Imaging and Signal Processing

Scanning was performed in a raster-scanning pattern, with B-line data acquired first along the x-axis, and the sample translated stepwise along the y-axis to complete the 2D scan. By stacking multiple B-line images in the y-direction, a full 3D volumetric dataset was reconstructed. Under the current system configuration, a representative 100 × 100 μm^2 FOV was acquired in approximately 30 s using x- and y-step sizes of 0.20 and 0.625 μm, respectively. Images of the same FOV were acquired under three scanning conditions with a fixed x-step size of 0.2 μm and y-step sizes of 0.625, 1.25, and 2.5 μm, corresponding to acquisition times of approximately 30, 15, and 8 s, respectively (Figure S10).

For organoid imaging, the average optical power at the sample was 0.3 mW at a repetition rate of 20 kHz, corresponding to a pulse energy of approximately 15 nJ. One laser pulse was used per pixel during raster scanning, resulting in an effective dwell time of 50 μs per pixel. Assuming a Gaussian excitation profile with a FWHM comparable to the measured lateral resolution (278 nm), the fluence averaged over the Gaussian $1/e^2$ beam area was estimated to be approximately 8.6 J/cm^2 per pulse. Because the optical focus was positioned within the organoid volume rather than at the tissue surface, the fluence at the organoid surface would be expected to be lower than the estimated focal plane fluence. To verify that the laser conditions did not induce immediate image changes, the same FOV was imaged four times under identical imaging conditions (Figure S11).

The acquired data were saved as binary files and post-processed using MATLAB software (MATLAB 2024, MathWorks, USA). A bandpass filter was applied to each A-line to suppress high- and low-frequency noise, followed by a Hilbert transform-based envelope detection to reconstruct the 3D volume. Finally, a MAP image was generated from the 3D data, and a 2D median filter was used to enhance image clarity. For the cross-sectional image (Figure 4f), different median-filter sizes were applied during B-mode image processing (7 × 7 for xz and 3 × 11 for yz) to ensure equivalent smoothing despite the different lateral sampling intervals between the xz and yz planes (0.5 μm in x and 2.5 μm in y). For resolution acquisition, the raw data were first converted to an envelope of the PA signal, after which a Gaussian fit was applied to obtain the lateral and axial FWHMs.

4.6 | Edge Detection Method for Cell Counting and Statistical Analysis

QuPath software (University of Edinburgh, UK) was used to conduct quantitative morphological analysis of cell nuclei [48]. The following cell detection parameters were applied to each image: background radius = 8 μm, median filter radius = 0 μm, sigma = 1.5 μm, minimum area = 5 μm^2, maximum area = 100 μm^2, and threshold = 50 a.u. According to these parameters, the nuclear area, equivalent diameter, and circularity were extracted for quantitative analysis.

To validate the reliability of the segmentation procedure used for nuclear morphology quantification, additional manual-versus-automated segmentation comparisons, object-level detection analyses, and threshold sensitivity assessments were performed using five control organoids (Figure S13). Manual masks were generated by manually annotating individual nuclear boundaries using the annotation tools available in QuPath, whereas automated masks were generated using the identical QuPath-based workflow and parameter settings employed for the nuclear morphology analyses presented in the original manuscript (Figure S13a). Segmentation performance was subsequently evaluated at

both the pixel and object levels. At the pixel level, automated nuclear segmentation showed strong agreement with manual annotations, yielding a Dice score of 0.93 ± 0.01, IoU of 0.87 ± 0.03, precision of 0.92 ± 0.02, and recall of 0.95 ± 0.02 across five image pairs (Figure S13b). Object-level analysis further demonstrated an average of 28.40 ± 6.23 true-positive detections, 4.40 ± 3.09 false-positive detections, and 2.00 ± 1.63 false-negative detections, corresponding to a precision of 0.88 ± 0.06, recall of 0.95 ± 0.04, and F1 score of 0.91 ± 0.05 (Figure S13b). Consistent with these pixel- and object-level results, no statistically significant differences were observed between manual and automated segmentation results for nuclear area, maximum caliper diameter, or circularity (Figure S13c). Despite occasional split, false-positive, or missed detections, the resulting nuclear morphology measurements remained statistically indistinguishable between the two segmentation approaches, indicating that the measured morphological parameters were not dependent on the segmentation method. To further evaluate sensitivity to segmentation settings, threshold values of 30, 40, 60, and 70 were additionally tested in both the control and EtOH groups, alongside the original threshold value of 50. Nuclear area, maximum caliper diameter, and circularity exhibited consistent trends across the tested threshold range, and the statistically significant differences between the control and EtOH groups were preserved under all threshold conditions (Figure S13d). Importantly, no threshold setting altered the overall biological interpretation of the results.

All statistical analyses were performed using a two-tailed unpaired parametric *t*-test provided by the GraphPad Prism (GraphPad Software, USA).

4.7 | Phantom Sample Preparation

To prepare the GNP phantom, 10 μL of GNPs were mixed with ultrasound gel to create a GNP-infused gel. For imaging, a thin layer of the GNP gel was spread on a quartz glass surface, and the transducer's focal distance was ensured using a membrane followed by water. The laser pulse energy was set to 20 nJ for GNP imaging, with a scan step size set to 50 nm per pixel. Assuming a speed of sound of 1500 m/s in water and a sampling rate of 500 MS/s, the digitizer's depth step size was estimated to be approximately 3 μm per pixel. Subsequently, to create the tilted carbon fiber phantom, one end of the carbon fiber was fixed to the quartz glass surface, while the other end was fixed on top of an additional 0.2 mm-thick quartz glass piece placed on the base layer. For this phantom, only water was used to maintain an appropriate focal distance of the transducer.

Author Contributions

L.V.W., J.K., J-C.P., and B.P. initiated and supervised the study. H.K. and W.J. conducted and designed the experiments. W.J. provided the cortical organoids. H.K. and W.J. analyzed the statistics. The manuscript was written with contributions from all authors. All the authors approved the final version of the manuscript.

Acknowledgements

This study was supported by the National Research Foundation (NRF) of Korea grants (RS-2021-NR060086, 2022R1C1C2012736, RS-2023-00266110, RS-2024-00462912, RS-2023-00210682, RS-2026-25522080, RS-2026-25472578) funded by the Ministry of Science and ICT (MSIT) of the Korean government; the Korea Dementia Research Project through the Korea Dementia Research Center (KDRC), the Ministry of Health & Welfare and MSIT, Republic of Korea (RS-2024-00339665). Figure 1 was created in BioRender. Kye, H. (2026). BioRender.com/xb079xr.

Funding

This study was supported by the National Research Foundation (NRF) of Korea grants (RS-2021-NR060086, 2022R1C1C2012736, RS-2023-00266110, RS-2024-00462912, RS-2023-00210682, RS-2026-25522080, RS-2026-25472578) funded by the Ministry of Science and ICT (MSIT) of the Korean government; the Korea Dementia Research Project through the Korea Dementia Research Center (KDRC), the Ministry of Health & Welfare and MSIT, Republic of Korea (RS-2024-00339665).

Conflicts of Interest

The authors declare no conflicts of interest.

Data Availability Statement

The data that support the findings of this study are available in the supplementary material of this article.

References

1. P. A. May, J. P. Gossage, W. O. Kalberg, et al., "Prevalence and Epidemiologic Characteristics of FASD From Various Research Methods With an Emphasis on Recent In-School Studies," *Developmental Disabilities Research Reviews* 15, no. 3 (2009): 176–192, https://doi.org/10.1002/ddrr.68.

2. T. Arzua, Y. Yan, C. Jiang, et al., "Modeling Alcohol-Induced Neurotoxicity Using Human Induced Pluripotent Stem Cell-derived Three-Dimensional Cerebral Organoids," *Translational Psychiatry* 10, no. 1 (2020): 347, https://doi.org/10.1038/s41398-020-01029-4.

3. P. A. May, J. M. Hasken, S. R. Hooper, et al., "Estimating the Community Prevalence, Child Traits, and Maternal Risk Factors of Fetal Alcohol Spectrum Disorders (FASD) From a Random Sample of School Children," *Drug and Alcohol Dependence* 227 (2021): 108918, https://doi.org/10.1016/j.drugalcdep.2021.108918.

4. H. M. Hwang, Y. I. Kawasawa, A. Basha, S. Mohammad, M. Ito, and K. Hashimoto-Torii, "Fatty Acid Metabolism Changes in Association With Neurobehavioral Deficits in Animal Models of Fetal Alcohol Spectrum Disorders," *Communications Biology* 6, no. 1 (2023): 736, https://doi.org/10.1038/s42003-023-05127-z.

5. X. Zeng, Y. Cai, M. Wu, H. Chen, M. Sun, and H. Yang, "An Overview of Current Advances in Perinatal Alcohol Exposure and Pathogenesis of Fetal Alcohol Spectrum Disorders," *Journal of Neurodevelopmental Disorders* 16, no. 1 (2024): 20, https://doi.org/10.1186/s11689-024-09537-w.

6. M. Olivares-Costa, M. C. Fabio, E. De la Fuente-Ortega, P. A. Haeger, and R. Pautassi, "New Therapeutics for the Prevention or Amelioration of Fetal Alcohol Spectrum Disorders: A Narrative Review of the Preclinical Literature," *The American Journal of Drug and Alcohol Abuse* 50, no. 6 (2024): 749–770, https://doi.org/10.1080/00952990.2024.2361442.

7. H. B. van der Worp, D. W. Howells, E. S. Sena, et al., "Can Animal Models of Disease Reliably Inform Human Studies?," *PLoS Medicine* 7, no. 3 (2010): 1000245.

8. R. D. Hodge, T. E. Bakken, J. A. Miller, et al., "Conserved Cell Types With Divergent Features in Human Versus Mouse Cortex," *Nature* 573, no. 7772 (2019): 61–68, https://doi.org/10.1038/s41586-019-1506-7.

9. A.-N. Cho, Y. Jin, Y. An, et al., "Microfluidic Device With Brain Extracellular Matrix Promotes Structural and Functional Maturation of Human Brain Organoids," *Nature Communications* 12, no. 1 (2021): 4730, https://doi.org/10.1038/s41467-021-24775-5.

10. A. Ramani, G. Pasquini, N. J. Gerkau, et al., "Reliability of High-Quantity Human Brain Organoids for Modeling Microcephaly, Glioma Invasion and Drug Screening," *Nature Communications* 15, no. 1 (2024): 10703, https://doi.org/10.1038/s41467-024-55226-6.

11. M. Ravi, V. Paramesh, S. Kaviya, E. Anuradha, and F. P. Solomon, "3D Cell Culture Systems: Advantages and Applications," *Journal of Cellular Physiology* 230, no. 1 (2015): 16–26, https://doi.org/10.1002/jcp.24683.

12. N. Sun, X. Meng, Y. Liu, D. Song, C. Jiang, and J. Cai, "Applications of Brain Organoids in Neurodevelopment and Neurological Diseases," *Journal of Biomedical Science* 28, no. 1 (2021): 30, https://doi.org/10.1186/s12929-021-00728-4.

13. S. Scuderi, G. G. Altobelli, V. Cimini, G. Coppola, and F. M. Vaccarino, "Cell-to-Cell Adhesion and Neurogenesis in Human Cortical Development: A Study Comparing 2D Monolayers With 3D Organoid Cultures," *Stem Cell Reports* 16, no. 2 (2021): 264–280, https://doi.org/10.1016/j.stemcr.2020.12.019.

14. J.-C. Park, S.-Y. Jang, D. Lee, et al., "A Logical Network-Based Drug-Screening Platform for Alzheimer's Disease Representing Pathological Features of Human Brain Organoids," *Nature Communications* 12, no. 1 (2021): 280, https://doi.org/10.1038/s41467-020-20440-5.

15. M. Notaras, A. Lodhi, E. Barrio-Alonso, et al., "Neurodevelopmental Signatures of Narcotic and Neuropsychiatric Risk Factors in 3D Human-Derived Forebrain Organoids," *Molecular Psychiatry* 26, no. 12 (2021): 7760–7783.

16. J. W. Adams, P. D. Negraes, J. Truong, et al., "Impact of Alcohol Exposure on Neural Development and Network Formation in Human Cortical Organoids," *Molecular Psychiatry* 28, no. 4 (2023): 1571–1584.

17. S. Park, C. H. Min, E. Choi, et al., "Long-Term Tracking of Neural and Oligodendroglial Development in Large-Scale Human Cerebral Organoids by Noninvasive Volumetric Imaging," *Scientific Reports* 15, no. 1 (2025): 2536, https://doi.org/10.1038/s41598-025-85455-8.

18. L. Gu, H. Cai, L. Chen, M. Gu, J. Tchieu, and F. Guo, "Functional Neural Networks in Human Brain Organoids," *BME Frontiers* 5 (2024): 0065, https://doi.org/10.34133/bmef.0065.

19. M. E. Lacin and M. Yildirim, "Applications of Multiphoton Microscopy in Imaging Cerebral and Retinal Organoids," *Frontiers in Neuroscience* 18 (2024): 1360482, https://doi.org/10.3389/fnins.2024.1360482.

20. E. Park, S. Misra, D. G. Hwang, et al., "Unsupervised Inter-Domain Transformation for Virtually Stained High-Resolution Mid-Infrared Photoacoustic Microscopy Using Explainable Deep Learning," *Nature Communications* 15, no. 1 (2024): 10892, https://doi.org/10.1038/s41467-024-55262-2.

21. K. R. Weiss, F. F. Voigt, D. P. Shepherd, and J. Huisken, "Tutorial: Practical Considerations for Tissue Clearing and Imaging," *Nature Protocols* 16, no. 6 (2021): 2732–2748, https://doi.org/10.1038/s41596-021-00502-8.

22. A. Barulin, E. Barulina, D. K. Oh, et al., "Axially Multifocal Metalens for 3D Volumetric Photoacoustic Imaging of Neuromelanin in Live Brain Organoid," *Science Advances* 11, no. 3 (2025): adr0654, https://doi.org/10.1126/sciadv.adr0654.

23. X. Luo, M. Chen, H. Shan, et al., "Label-Free 3D Photoacoustic Imaging of Tumor Organoids for Volumetric Drug Screening," *Advanced Science* 12 (2025): 17226.

24. M. Xu and L. V. Wang, "Photoacoustic Imaging in Biomedicine," *Review of Scientific Instruments* 77, no. 4 (2006): 041101, https://doi.org/10.1063/1.2195024.

25. M. V. Novoselova, T. O. Abakumova, B. N. Khlebtsov, et al., "Optical Clearing for Photoacoustic Lympho-and Angiography Beyond Conventional Depth Limit In Vivo," *Photoacoustics* 20 (2020): 100186, https://doi.org/10.1016/j.pacs.2020.100186.

26. H. Li, M. Sun, B. Zhu, et al., "Multidimensional Dynamic Optical Imaging Unveils Anesthetic-Driven Hemispheric Lateralization in Blood-Brain Barrier Homeostasis," *Science Advances* 11, no. 49 (2025): ady6275, https://doi.org/10.1126/sciadv.ady6275.

27. W. Qin, H. Li, J. Chen, Y. Qiu, L. Ma, and L. Nie, "Amphiphilic Hemicyanine Molecular Probes Crossing the Blood-Brain Barrier for Intracranial Optical Imaging of Glioblastoma," *Science Advances* 11, no. 3 (2025): adq5816, https://doi.org/10.1126/sciadv.adq5816.

28. S.-W. Cho, T. T. V. Phan, S. M. Park, H. Lee, J. Oh, and C.-S. Kim, "Efficient Label-Free In Vivo Photoacoustic Imaging of Melanoma Cells Using a Condensed NIR-I Spectral Window," *Photoacoustics* 29 (2023): 100456, https://doi.org/10.1016/j.pacs.2023.100456.

29. H. Kye, M. S. Kang, D. Jo, et al., "Advances in High-Resolution Photoacoustic Imaging Techniques for Cellular Visualization," *View* 7 (2025): 20250125.

30. X. Zhu, Q. Huang, A. DiSpirito, et al., "Real-Time Whole-Brain Imaging of Hemodynamics and Oxygenation at Micro-Vessel Resolution With Ultrafast Wide-Field Photoacoustic Microscopy," *Light: Science & Applications* 11, no. 1 (2022): 138, https://doi.org/10.1038/s41377-022-00836-2.

31. J. Park, B. Park, T. Y. Kim, et al., "Quadruple Ultrasound, Photoacoustic, Optical Coherence, and Fluorescence Fusion Imaging With a Transparent Ultrasound Transducer," *Proceedings of the National Academy of Sciences* 118, no. 11 (2021): 1920879118, https://doi.org/10.1073/pnas.1920879118.

32. T. T. Wong, R. Zhang, P. Hai, et al., "Fast Label-Free Multilayered Histology-Like Imaging of Human Breast Cancer by Photoacoustic Microscopy," *Science Advances* 3, no. 5 (2017): 1602168.

33. N. J. Haven, K. L. Bell, P. Kedarisetti, J. D. Lewis, and R. J. Zemp, "Ultraviolet Photoacoustic Remote Sensing Microscopy," *Optics Letters* 44, no. 14 (2019): 3586, https://doi.org/10.1364/OL.44.003586.

34. W. Song, C. Guo, Y. Zhao, et al., "Ultraviolet Metasurface-Assisted Photoacoustic Microscopy With Great Enhancement in DOF for Fast Histology Imaging," *Photoacoustics* 32 (2023): 100525, https://doi.org/10.1016/j.pacs.2023.100525.

35. D. Kim, E. Park, J. Park, et al., "An Ultraviolet-Transparent Ultrasound Transducer Enables High-Resolution Label-Free Photoacoustic Histopathology," *Laser & Photonics Reviews* 18, no. 2 (2024): 2300652, https://doi.org/10.1002/lpor.202300652.

36. J. W. Baik, H. Kim, M. Son, et al., "Intraoperative Label-Free Photoacoustic Histopathology of Clinical Specimens," *Laser & Photonics Reviews* 15, no. 10 (2021): 2100124, https://doi.org/10.1002/lpor.202100124.

37. P. Mateos-Martínez, R. Coronel, M. Sachse, et al., "Human Cerebral Organoids: Cellular Composition and Subcellular Morphological Features," *Frontiers in Cellular Neuroscience* 18 (2024): 1406839, https://doi.org/10.3389/fncel.2024.1406839.

38. J. R. Eidet, L. Pasovic, R. Maria, C. J. Jackson, and T. P. Utheim, "Objective Assessment of Changes in Nuclear Morphology and Cell Distribution Following Induction of Apoptosis," *Diagnostic Pathology* 9, no. 1 (2014): 92, https://doi.org/10.1186/1746-1596-9-92.

39. R. Cao, J. Zhao, L. Li, et al., "Optical-Resolution Photoacoustic Microscopy With a Needle-Shaped Beam," *Nature Photonics* 17, no. 1 (2023): 89–95, https://doi.org/10.1038/s41566-022-01112-w.

40. X. Zhu, L. Menozzi, S.-W. Cho, and J. Yao, "High Speed Innovations in Photoacoustic Microscopy," *NPJ Imaging* 2, no. 1 (2024): 46.

41. T. Wang, J. Chen, L. Nie, and H. Li, "Photoacoustic Microscopy for Multiscale Biological System Visualization and Clinical Translation," *Advanced Science* 13, no. 9 (2026): 21173.

42. J. Y. Kim, C. Lee, K. Park, G. Lim, and C. Kim, "Fast Optical-Resolution Photoacoustic Microscopy Using a 2-Axis Water-Proofing MEMS Scanner," *Scientific Reports* 5, no. 1 (2015): 7932, https://doi.org/10.1038/srep07932.

43. A. Barulin, H. Park, B. Park, and I. Kim, "Dual-Wavelength UV-Visible Metalens for Multispectral Photoacoustic Microscopy: A Simulation Study," *Photoacoustics* 32 (2023): 100545, https://doi.org/10.1016/j.pacs.2023.100545.

44. R. Cao, S. D. Nelson, S. Davis, et al., "Label-Free Intraoperative Histology of Bone Tissue via Deep-Learning-Assisted Ultraviolet Photoacoustic Microscopy," *Nature Biomedical Engineering* 7, no. 2 (2023): 124–134, https://doi.org/10.1038/s41551-022-00940-z.

45. S. Zhang, J. Li, L. Shen, et al., "Structure and Oxygen Saturation Recovery of Sparse Photoacoustic Microscopy Images by Deep Learning," *Photoacoustics* 42 (2025): 100687, https://doi.org/10.1016/j.pacs.2025.100687.

46. V. Gorti, K. McCubbins, D. Houston, et al., "Quantifying UV-Induced Photodamage for Longitudinal Live-Cell Imaging Applications of Deep-UV Microscopy," *Biomedical Optics Express* 16, no. 1 (2024): 208, https://doi.org/10.1364/BOE.544778.

47. J. Pawley, *Handbook of Biological Confocal Microscopy* (Springer Science & Business Media, 2006), https://doi.org/10.1007/978-0-387-45524-2.

48. P. Bankhead, M. B. Loughrey, J. A. Fernández, et al., "QuPath: Open Source Software for Digital Pathology Image Analysis," *Scientific Reports* 7, no. 1 (2017): 1–7, https://doi.org/10.1038/s41598-017-17204-5.

Supporting Information

Additional supporting information can be found online in the Supporting Information section.

Supporting File 1: smll74598-sup-0001-SuppMat.docx.

Supporting File 2: smll74598-sup-0002-MovieS1.avi.